 CMES, vol.33, no.3, pp.269-292, 2008

Numerical Simulations of Dynamic Fracture in Thin Shell Structures

C. Gato and Y. Shie[1]

Abstract: Numerical simulations of large deformation dynamic fracture in thin shell structures using 3-D meshfree method is presented. Due to the smoothness of the meshfree shape functions, they are well suited to simulate large deformation of thin shell structures while avoiding ill-conditioning as well as stiffening in numerical computations. Dynamic fracture is modeled by simple criterion, i.e. removing connectivity between adjacent nodes once a fracture criterion is met. The main advantage of such 3-D meshfree continuum approach is its simplicity in both formulation and implementation as compared to shell theory approach, or degenerated continuum approach. Moreover, it is believed that the accuracy of the computation may increase because of using 3-D exact formulation.

Keyword: fracture, shell, meshfree

1 Introduction

The numerical simulation of thin shell structures has been a challenge in applied mechanics and in many engineering branches for many years. Its engineering significance as well as technical difficulties can be best measured by the seemingly ever-lasting 'new formulations' or 'new contributions' in the literature in the past decades. Its applications cover e.g. sheet metal forming, crash-worthiness test, civil structure design, pressure vessel liability, shipbuilding, defense technology, just to name a few. Regarding the strategy of numerical simulations of thin shell structures, there are three major approaches:

1. numerical simulation based on shell theories
2. degenerated continuum, or continuum based approach
3. direct three-dimensional (3-D) continuum approach

[1] Harbin Engineering University College of Mechanical Engineering Harbin, HLJ, P.R.China

Among these three approaches, 3-D continuum direct approach is the simplest; nonetheless it is the least popular one in practice. The major drawback, or dilemma that prevents using 3-D direct simulation is that it is often required to deploy multiple elements in the thickness direction of the thin shell to acquire reasonable gradient fields, which, on the other hand, leads to degrading the conditioning of the discrete system and then the accuracy of the numerical solution; moreover, the direct continuum approach is very expensive, which usually requires more elements in the same simulation than shell theory approach, or degenerated approach does.

Most meshfree methods proposed so far have focused on a continuum-based approach or simply modeled the shell or plate as a standard continuum. A meshfree thin shell formulation based on Kirchhoff-love theory and element-free Galerkin (EFG) method Belytschko, Lu, and Gu (1994) has been developed by Krysl and Belytschko (1996) in the context of small strain, linear elastic framework. Rabczuk, Areias, and Belytschko (2007) extended this work with the consideration of finite strain, non-linear elastic material and focused on fracture. In the following work, Rabczuk and Areias (2006) have simplified the treatment of cracks in thin shell by using an extrinsic basis. Donning and Liu (1998) noted the advantage of meshfree approximations in addressing shear locking in Mindlin type of beams and plates and have developed a meshfree formulation based on the reproducing kernel particle method (RKPM) Liu, Jun, and Zhang (1995). This methodology is further extended by Kanok-Nukulchai, Barry, Saran-Yasoontorn, and Bouillards (2001) with the use of EFG. EFG has been employed by Noguchi, Kawashima, and Miyamura (2000) for shell and membrane structures in which bi-cubic and quartic basis functions are introduced in order to avoid shear and membrane locking. Leitao (2001) developed a meshfree method based on radial basis functions (RBF) for modeling a Kirchhoff type of plate. Extension of RBF approach to the Mindlin type of plate was presented in Liew and Chen (2004b,a). The meshless local Petrov-Galerkin was proposed by Atluri and Zhu (1998, 2000); Atluri and Shen (2002); Atluri (2002); Han and Atluri (2003); Tang, Shen, and Atluri (2003); Liu, Han, Rajendran, and Atluri (2006) for solving beam problems and application of this meshfree approach to plates and shells can be found in Long and Atluri (2002); Atluri, Cho, and Kim (1999); Soric, Li, Jarak, and Atluri (2004); Sladek, Sladek, Wen, and Aliabadi (2006); Jarak, Soric, and Hostler (2007); Li, Soric, Jarak, and Atluri (2005); Andreaus, Batra, and Porfiri (2005); Sladek, Sladek, and Solek (2008); Jiawei, Xuefeng, and Lianfa (2008). Wang and Chen (2006) showed that the Kirchhoff mode in the Mindlin plate can be reproduced using EFG or RKPM if second-order polynomial basis is used in the moving least-squares approximation. By implementing this with a nodal integration and stabilization scheme, they have shown that the formulation is stable and free of shear locking. Yagawa and Miyamura (2005) developed a free mesh method in which the discrete Kirchhoff theory is combined with the mixed approach. In the case of 3D continuum models, Li, Hao, and Liu (2000) have presented a formulation based on RKPM and have studied non-linear large deformation of thin shells. Other relevant literature related to fracture or shell theory are given e.g. in Hao and Liu (1999); Hao, Liu, and Chang (2000); Guz, Menshykov, and Zozulya (2007); Ju and Liu (2007); Rabczuk and Belytschko (2006); Hagihara, Tsunori, and Ikeda (2007); Nishioka, Kobayashi, and Fujimoto (2007); Hao, Liu, and Weertman (2004); Liu, Liu, and Mahadevan (2007); Hao, Liu, Moran, Vernerey, and Olson (2004); Guo and Nairn (2006); Zhao, Liu, and Wu (2008); Rabczuk and Zi (2007); Ma, Lu, and Wang (2006); Gao, Liu, and Liu (2006); Hao, Liu, Moran, and Olson (2003); Hao, Liu, Klein, and Rosakis (2004); Rong, Huang, Liu, Song, and Wang (2008); Hao, Liu, and Belytschko (2004); Rabczuk, PMA, and Belytschko (2007); Fujimoto and Nishioka (2006); Nishioka (2005); Hao and Liu (2006); Nguyen-Van, N, and Tran-Cong (2008); Le, Mai-Duy, and Tran-Cong (2008).

In this paper, we use meshfree 3-D continuum approach based on simple fracture criterion. Once fracture criterion is met, connectivity between meshfree nodes are removed. The advantage of this 3-D meshfree approach is its simplicity over more complex methods.

The paper is structured as follows: We first describe the meshfree approximation and the discrete equations. Then, we elaborate the fracture criterion. Two problems involving large deformation dynamic fracture of thin shell structures are studied. At the end, we conclude our paper and give future research directions.

2 General formulation

We have used a formulation within the total Lagrangian framework. Conservation of linear momentum can be written as

$$\nabla_X \cdot \mathbf{P} + \rho_0 \mathbf{b} \quad = \quad \rho_0\, \ddot{\mathbf{u}}, \quad \mathbf{X} \in \Omega_0 \tag{1}$$

where $\mathbf{b}$ is the body force, ρ_0 is initial density, $\mathbf{u}$ is displacement, $\mathbf{P}$ is the first Piola-Kirchhoff stress tensor, ∇_X denotes spatial derivatives with respect to material coordinate and superimposed dots denote material time derivatives. The weak formulation of linear momentum equation is: Find $\mathbf{u} \in \mathscr{U}$ and $\delta\mathbf{u} \in \mathscr{U}_0$ such that

$$\delta W = \delta W_{int} - \delta W_{ext} + \delta W_{kin} = 0 \tag{2}$$

with

$$
\begin{aligned}
\delta W_{int} &= \int_{\Omega_0} \nabla_X \delta \mathbf{u} : \mathbf{P}\, d\Omega_0 \\
\delta W_{ext} &= \int_{\Gamma_{0t}} \delta \mathbf{u} \cdot \bar{\mathbf{t}}_0\, d\Gamma_0 + \int_{\Omega_0} \rho_0 \delta \mathbf{u} \cdot \mathbf{b}\, d\Omega_0 \\
\delta W_{kin} &= \int_{\Omega_0} \rho_0 \delta \mathbf{u} \cdot \ddot{\mathbf{u}}\, d\Omega_0
\end{aligned} \tag{3}
$$

with the approximation spaces $\mathscr{U}$ and $\mathscr{U}_0$ for the trial and test functions, respectively,

$$
\begin{aligned}
\mathscr{U} &= \left\{ \mathbf{u} | \mathbf{u} \in H^1,\ \mathbf{u} = \bar{\mathbf{u}}\ on\ \Gamma_u \right\} \\
\mathscr{U}_0 &= \left\{ \delta\mathbf{u} | \delta\mathbf{u} \in H^1,\ \delta\mathbf{u} = 0\ on\ \Gamma_u \right\}
\end{aligned} \tag{4}
$$

The linear momentum equation is complemented with Dirichlet and von Neumann boundary conditions:

$$\mathbf{u} = \bar{\mathbf{u}}, \quad \mathbf{X} \in \Gamma_{Xu} \tag{5}$$

$$\mathbf{n}_0 \cdot \mathbf{P} = \mathbf{t}_0 = \bar{\mathbf{t}}_0, \quad \mathbf{X} \in \Gamma_{0t} \tag{6}$$

where the index t refers to traction boundaries, the index u refers to displacement boundaries; $\mathbf{n}$ is the normal to the traction boundary and the subscript 0 refers to quantities in the reference configuration; $\mathbf{t}$ is the traction.

3 Meshfree approximation

We use the elementfree Galerkin (EFG) method Belytschko, Lu, and Gu (1994) that is based on moving least squares (MLS) Lancaster and Salkauskas (1981) approximation. The EFG approximation $\mathbf{u}^h(\mathbf{X})$ of a given function $\mathbf{u}(\mathbf{X})$ can be posed in terms of the shape functions and certain particle or nodal parameters $\mathbf{u}_J$ as

$$\mathbf{u}^h(\mathbf{X}) = \sum_{J=1}^{n} N_J(\mathbf{X})\mathbf{u}_J = \mathbf{N}\,\mathbf{u} \tag{7}$$

with n particles and shape functions

$$\mathbf{N}^T(\mathbf{X}) = \mathbf{p}^T(\mathbf{X})\mathbf{A}^{-1}(\mathbf{X})\mathbf{P}\mathbf{W}(\mathbf{X}) \tag{8}$$

where $\mathbf{A}$ is the moment matrix with moment matrix

$$\mathbf{A}(\mathbf{X}) = \mathbf{P}(\mathbf{Y})W(\mathbf{X})\mathbf{P}^T(\mathbf{Y}) \tag{9}$$

where the matrix $\mathbf{P}^T(\mathbf{Y})$ contains the polynomial basis $\mathbf{p}$ and

$$\mathbf{W}(\mathbf{X}) = diag\{W_I(\mathbf{X}-\mathbf{X}_I,h)V_I\}\,,\ I=1,...,n \tag{10}$$

$W_I(\mathbf{X}-\mathbf{X}_I,h)$ is a kernel function with compact support, its parameter h, usually called smoothing length or dilation parameter is a certain characteristic measure of the size of the support of the kernel function (e.g. the radius in circular supports). We used the quartic spline function that is commonly used in the literature:

$$W(\mathbf{X}-\mathbf{X}_I,h) \quad = \quad w(s) = \begin{cases} 1-6s^2+8s^3-3s^4 & s \leq 1 \\ 0 & s > 1 \end{cases} \tag{11}$$

with $s = \frac{\mathbf{X}-\mathbf{X}_I}{2h}$ for circular support size. The size of the domain of influence is connected to the nodal spacing. We consider only structured nodal arrangements Rabczuk and Belytschko (2005). The support size of the domain of influence, i.e. the radius of the support size is twice the particle spacing, figure 1. Such support sizes are commonly used in meshfree methods **?**. The matrix $\mathbf{P}$ contains the polynomial basis $\mathbf{p}$. Instead of the global polynomial basis $\mathbf{p}(\mathbf{Y})$, we use a scaled locally defined polynomial basis $\mathbf{p}((\mathbf{Y}-\mathbf{X})/h)$, that leads to better conditioned moment matrix $\mathbf{A}$. In this work, we use a quadratic polynomial basis. We note that the EFG approximation does not fulfil the Kronecker-delta property, i.e. $\mathbf{u}(\mathbf{X}_I) \neq \mathbf{u}_I$. This requires specific attention when imposing displacement boundary conditions. Also, if for example the displacement field needs to be plotted, then eq. (7) needs to be used in the post-processing. More details on the EFG method can be found in the literature Belytschko, Lu, and Gu (1994); **?**.

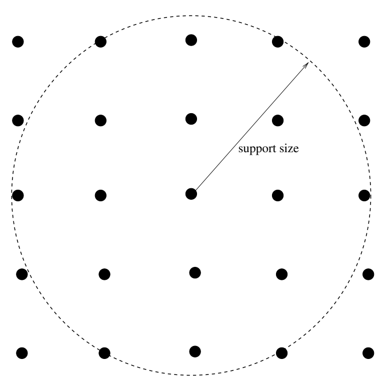

(a)

Figure 1: Radial support size

The test and trial functions have the structure of equation (7). Introducing them into the weak formulation with a Bubnov Galerkin method yields

$$\sum_{I=1}^{n} \delta \mathbf{u}_I \left\{ \sum_{J=1}^{n} - \int_{\Omega_0} \nabla_X N_I(\mathbf{X}) \mathbf{P} \, d\Omega_0 + \int_{\Omega_0} N_I(\mathbf{X}) \mathbf{b} \, d\Omega_0 \right.$$

$$\left. + \int_{\Gamma_{0t}} N_I(\mathbf{X}) \bar{\mathbf{t}}_0 \, d\Gamma_0 + \int_{\Omega_0} \rho_0 N_I(\mathbf{X}) N_J(\mathbf{X}) \mathbf{u} \, d\Omega_0 \right\} = 0 \tag{12}$$

Thus, for each particle I, the following identity must hold

$$\sum_{J=1}^{n} \int_{\Omega_0} \nabla_X N_I(\mathbf{X}) \mathbf{P} \, d\Omega_0 = \int_{\Omega_0} N_I(\mathbf{X}) \mathbf{b} \, d\Omega_0$$

$$+ \int_{\Gamma_{0t}} N_I(\mathbf{X}) \bar{\mathbf{t}}_0 \, d\Gamma_0 + \int_{\Omega_0} \rho_0 N_I(\mathbf{X}) N_J(\mathbf{X}) \mathbf{u} \, d\Omega_0 = 0 \tag{13}$$

These equations can be recast into a matrix form

$$\mathbf{M}_{IJ} \ddot{\mathbf{u}}_J = -\mathbf{f}_I^{ext} + \mathbf{f}_I^{int} \tag{14}$$

with

$$\mathbf{M}_{IJ} = \int_{\Omega_0} \rho \mathbf{N}_I(\mathbf{X}) \, \mathbf{N}_J^T(\mathbf{X}) \, d\Omega_0$$

$$\mathbf{f}_I^{ext} = \int_{\Gamma_{0t}} \mathbf{N}_I^T(\mathbf{X}) \, \bar{\mathbf{t}}_0 d\Gamma_0 + \int_{\Omega_0} \mathbf{N}_I^T(\mathbf{X}) \, \mathbf{b} d\Omega_0 \tag{15}$$

$$\mathbf{f}_I^{int} = \int_{\Omega_0} \nabla_X \mathbf{N}_I^T \mathbf{X}) \, \mathbf{P} d\Omega_0 \tag{16}$$

The domain is subdivided into integration domains over which Gaussian quadrature is performed. Background mesh is constructed such that nodes and integration cell vertices coincide, see figure 2 for a two-dimensional description. We note that the background mesh does not necessarily have to be conforming and hanging nodes may easily be employed. Using Gaussian quadrature, the internal forces for examples are given by Rabczuk, Belytschko, and Xiao (2004)

$$\mathbf{f}_I^{int} = \sum_{J=1} n \nabla_X N(\mathbf{X}(\xi_J) - \mathbf{X}_I) \, \mathbf{P}(\mathbf{X}(\xi_J)) \, w_J^Q |\mathbf{J}| \tag{17}$$

where ξ are local coordinates of the background mesh, $|\mathbf{J}|$ is the determinant of the Jacobian and w_J^Q are the quadrature weights.

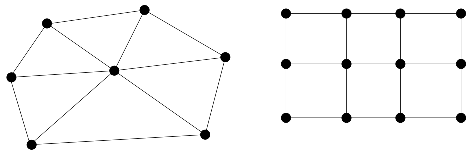

(a)

Figure 2: EFG nodes plotted as circular black dots with background mesh; left side: unstructured mesh and right side: structured mesh

4 Constitutive model and Failure criterion

4.1 Visoplasticity model

We use a J_2 isotropic hardening viscoplastic model of the type

$$g(\varepsilon^p) = \sigma_0 \left(1 + \frac{\varepsilon^p}{\varepsilon_0^p}\right)^{1/n} \tag{18}$$

where σ_0 is yield stress, ε^p and ε_0^p are the total and reference plastic strains, respectively and $1/n$ is hardening exponent.

Rate dependent behavior is modeled with power law of type

$$\sigma_{eff} = g(\varepsilon^p) \left(1 + \frac{\dot{\varepsilon}^p}{\dot{\varepsilon}_0^p}\right)^{1/m} \tag{19}$$

where $1/m$ is reference plastic strain rate and $1/m$ is strain rate sensitivity exponent.

4.2 Thermo-viscoplastic model

In this section, we outline the constitutive relation of the thermo-elasto-viscoplastic solid adopted from Zhou, Ravichandran, and Rosakis (1996) in order to evaluate the stress term in Equation 2. The rate form of the constitutive equation reads as follows:

$$\tau^{\nabla} = \mathbf{C} : \left(\mathbf{D} - \mathbf{D}^{vp} - \alpha \dot{T} \mathbf{I}\right) \tag{20}$$

where $\mathbf{C}$ is the first order elasticity tensor, $\mathbf{D}$ is the symmetric part of the velocity gradient $\mathbf{L}$, $\tau^{\nabla} = \dot{\tau} - \mathbf{W} \cdot \tau - \tau \cdot \mathbf{W}$ is the Jaumann rate of the Kirchhoff stress where $\mathbf{W}$ is the antimetric part of the velocity gradient, α is the thermal expansion coefficient and $\mathbf{I}$ is the second-order identity matrix. The viscoplastic overstress model here is based on von Mises

$$\mathbf{D}^{vp} = \left(\frac{3\dot{\bar{\varepsilon}}}{2\bar{\sigma}}\right) \tilde{\mathbf{s}} \tag{21}$$

with

$$\tilde{\mathbf{s}} = \mathbf{s} - \mathbf{a} \ \text{ with } \mathbf{s} = \tau - 1/3tr(\tau)\,\mathbf{I},\ \bar{\sigma} = 3/2\tilde{\mathbf{s}} : \tilde{\mathbf{s}} \tag{22}$$

where **a** is the back stress, set to zero in our studies. The thermo viscoplastic flow is governed by the following power law

$$\dot{\bar{\varepsilon}} = \dot{\varepsilon}_0 \left(\frac{\bar{\sigma}}{g(\bar{\varepsilon}, T)} \right)^m \tag{23}$$

with

$$g(\bar{\varepsilon}, T) = \bar{\sigma} \left(1 + \frac{\bar{\varepsilon}}{\varepsilon_0} \right)^n \left(1 - \delta \left[exp\left(\frac{T - T_0}{\kappa} \right) - 1 \right] \right) \tag{24}$$

In Equations (23) and (24), $\dot{\varepsilon}_0$ is a reference strain rate, m is the rate sensitivity parameter, σ_0 is the yield stress, $\varepsilon_0 = \sigma_0/E$ is the corresponding reference strain and E is Young's modulus, n is the strain hardening exponent, T_0 is a reference temperature and δ and κ are thermal softening parameters. The function $g(\bar{\varepsilon}, T)$ is the stress-strain relation measured at quasi-static strain rate of $\dot{\varepsilon}$ at temperature T . The equivalent plastic strain $\bar{\varepsilon}$ is defined as

$$\bar{\varepsilon} = \int_0^t \dot{\bar{\varepsilon}}\, dt = \int_0^t \sqrt{\frac{2}{3}\mathbf{D}^{vp} : \mathbf{D}^{vp}}\, dt \tag{25}$$

Softening in material due to temperature is accounted for by varying material parameters

$$\begin{aligned}
E(T) &= E_0 - 1.6 \times 10^6 (T - T_0) - 10^5 \left(T - T_{)}\right)\ [Pa] \\
\nu &= \nu_0 + 5 \times 10^{-5} (T - T_0) \\
\sigma_0(T) &= \sigma_0 - 1.5 \times 10^3 (T - T_0)^2\ [Pa] \\
\alpha(T) &= (2.2 + 0.0016\,[T - T_0]) \times 10^{-5}\ [K^{-1}]
\end{aligned} \tag{26}$$

where E and ν are Young's modulus and the Poisson ratio at temperature T. Furthermore, for steel: E_0= 200GPa, ν_0=0.3 and σ_0=2.0GPa. The constitutive update scheme for the thermo-elasto-viscoplastic model largely follows the rate tangent modulus approach developed by Peirce, Shih, and Needleman (1984). The essence of the rate tangent modulus method is to approximate any function of time in the interval $t_{n+\theta} \in [t_n, t_{n+1}]$, $\theta \in [0,1]$ as

$$f_\theta = (1 - \theta)\, f_n + \theta f_{n+1} \tag{27}$$

Thus, with the predicted velocity field $\mathbf{v}_{n+1}^{trial} = \mathbf{v}_n + \Delta t\ \mathbf{a}_n$ it follows that

$$\mathbf{v}_\theta = (1-\theta)\,\mathbf{v}_n + \theta \mathbf{v}_{n+1}^{trial} = \mathbf{v}_n + \theta \Delta t\ \mathbf{a}_n \tag{28}$$
$$\mathbf{u}_\theta = (1-\theta)\,\mathbf{u}_n + \theta \mathbf{u}_{n+1} = \mathbf{u}_n + \theta \Delta t\ \mathbf{v}_n + \theta^2 \Delta t^2\ \mathbf{a}_n \tag{29}$$
$$\mathbf{L}_\theta = \nabla_X \mathbf{v}_\theta \cdot \mathbf{F}_{n+1}^{-1} \tag{30}$$

With $\theta = 0.5$, we recovered central difference scheme. To update the Kirchhoff stress, we proceed as follows:

$$\tau_{n+1} = \tau_n + \dot{\tau}\ \Delta t \tag{31}$$
$$\dot{\tau} \approx \tau^{\nabla} + \mathbf{W}_\theta \cdot \tau_n + \tau_n \cdot \mathbf{W}_\theta^T \tag{32}$$

Of course, one has to find first $\dot{\bar{\varepsilon}}_\theta$ before τ^{∇}. Let

$$\dot{\bar{\varepsilon}}_\theta = (1-\theta)\,\dot{\bar{\varepsilon}}_n + \theta \dot{\bar{\varepsilon}}_{n+1} \tag{33}$$

where $\dot{\bar{\varepsilon}}_{n+1}$ is approximated by a first-order Taylor series expansion in $\bar{\sigma}$, $\bar{\varepsilon}$ and T

$$\dot{\bar{\varepsilon}}_{n+1} = \dot{\bar{\varepsilon}}_n + \Delta t_n \left(\frac{\partial \dot{\bar{\varepsilon}}}{\partial \bar{\sigma}}|_n \dot{\bar{\sigma}}_\theta + \frac{\partial \dot{\bar{\varepsilon}}}{\partial \bar{\varepsilon}}|_n \dot{\bar{\varepsilon}}_\theta + \frac{\partial \dot{\bar{\varepsilon}}}{\partial T}|_n \dot{T}_\theta \right) \tag{34}$$

Assume that the temperature update proceeds first, and $\dot{T}_\theta$ comes in handy; based on plastic consistency condition and constitutive relations, on may find that

$$\dot{\bar{\varepsilon}}_\theta \approx \frac{\dot{\bar{\varepsilon}}_n}{1+\zeta_\theta} + \frac{\zeta_\theta}{H_\theta\,(1+\zeta_\theta)} \left(\mathbf{P}_\theta : \mathbf{D}_\theta + \dot{T}_\theta \left(\frac{\partial \dot{\bar{\varepsilon}}/\partial T}{\partial \dot{\bar{\varepsilon}}/\partial \bar{\sigma}} \right)_n \right) \tag{35}$$

where

$$\mathbf{P}_\theta = \mathbf{C} : \mathbf{p}_n \tag{36}$$
$$\mathbf{p}_n = \frac{3\tilde{\mathbf{s}}}{2\bar{\sigma}} \tag{37}$$
$$H_\theta \approx \frac{\partial \dot{\bar{\varepsilon}}/\partial \bar{\varepsilon}}{\partial \dot{\bar{\varepsilon}}/\partial \bar{\sigma}}|_n + (\mathbf{p} : \mathbf{L} : \mathbf{p})_n \tag{38}$$
$$\zeta_\theta \approx \theta\ \Delta t \left(\frac{\partial \dot{\bar{\varepsilon}}}{\partial \bar{\sigma}} \right)_n H_\theta \tag{39}$$
$$\frac{\partial \dot{\bar{\varepsilon}}}{\partial \bar{\sigma}} = \frac{m \dot{\bar{\varepsilon}}}{\bar{\sigma}} \tag{40}$$
$$\frac{\partial \dot{\bar{\varepsilon}}/\partial T}{\partial \dot{\bar{\varepsilon}}/\partial \bar{\sigma}}|_n = -\left(\frac{\bar{\sigma}}{g(\bar{\varepsilon}, T)} \right) \frac{\partial g}{\partial T} \tag{41}$$

Following the rate tangent modulus approach Peirce, Shih, and Needleman (1984), the objective rate of the Kirchhoff stress can be given as

$$\tau^{\nabla} = \mathbf{C}_{\theta}^{tan} : \mathbf{D}_{\theta} - \frac{\dot{\bar{\varepsilon}}_n}{1+\zeta_\theta}\mathbf{P}_\theta - \frac{\zeta_\theta}{(1+\zeta_\theta)H_\theta}\frac{\partial\dot{\bar{\varepsilon}}/\partial T}{\partial\dot{\bar{\varepsilon}}/\partial\bar{\sigma}}|_n \dot{T}_\theta \mathbf{P}_\theta - \alpha\dot{T}_\theta \mathbf{C} : \mathbf{I} \tag{42}$$

where

$$\mathbf{C}_{\theta}^{tan} = \mathbf{C} - \left(\frac{\zeta}{(1+\zeta)H}\right)_\theta \mathbf{P}_\theta : \mathbf{P}_\theta \tag{43}$$

Once the objective rate is obtained, the Kirchhoff stress can then be updated according to Equation(31). The corresponding first Piola Kirchhoff stress tensor is then given as $\mathbf{P} = \mathbf{F}^{-1} \cdot \tau$.

4.3 Failure model

Two types of failure models are used

- Stress-based fracture criterion
- Strain-based fracture criterion

For stress-based fracture criterion, fracture is introduced once the maximum principal tensile stress exceed 3 times the tensile strength σ_0 of the material.

For strain-based fracture criterion, fracture is introduced once the effective plastic strain rate exceeds a given threshold. This threshold is 0.2 in our studies.

Both criteria required a non-local averaging of stress and strain field.

Fracture is modeled in a very simple manner. We broke the link between neighboring particles once fracture criterion is met. More sophisticated models will be studied in the future.

5 Results

5.1 Pinched cylinder

We first show the efficiency and accuracy of the method with simple example: Linear elastic pinched cylinder with rigid end diaphragm. This problem resembles one of bench mark problems in the so-called standard problem set testing finite element accuracy and was tested for example by Sze, Lo, and Yao (2002); Weissmann

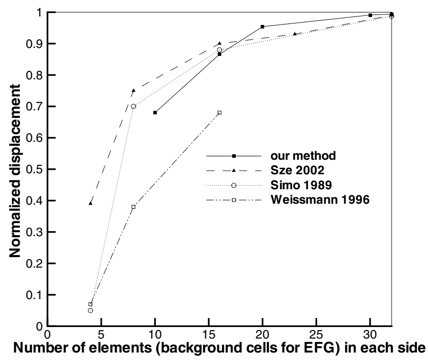

(a)

Figure 3: Normalized displacement versus number of elements in each side, pinched cylinder example

(1996); Bucalem and Bathe (1993); Parish (1991); Simo, Fox, and Rifai (1989). Only one eights of the cylinder is usually modeled. We model the entire cylinder since we cannot take advantage of symmetry in the following examples. In order to compare results with the literature, we have scaled the number of background cells to the number of elements of the $1/8$ cylinder. This normalized displacement plot is depicted in figure 3. The results are of similar accuracy as results with finite elements that use the same number of elements though this method is much simpler and better suited for modeling fracture.

5.2 Cylinder under internal pressure

The configuration of the problem is shown in Figure 4. The cylinder considered has an axial length of 1.2m. The circular cross-section has a mean radius of 22.575 cm and thickness of 0.15 cm. The mesh for approximately 30,000 nodes is shown in figure 5a. The finer mesh with approximately 150,000 nodes is shown in figure 5b. The background cells built by 4 nodes are illustrated in this figure as well. We used standard commercial software to obtain the nodal points and the background mesh. We also used a mesh with 100,000 nodes and 120,000 nodes.

The initial crack is modeled with the visibility criterion developed Belytschko and Lu (1995); Belytschko, Lu, and Gu (1995). Thermo-viscoplastic model described in section 4.2 is used with material parameters: $\dot{\varepsilon}_0 = 0.001s^{-1}$, $m = 70$, $n = 0.01$, $T_0 = 293K$, $\delta = 0.5$, $\kappa = 1000K$, $\rho = 7839kg/m^3$, $c_p = 448J/(kgK)$, $\chi = 0.9$. Stress-based fracture criterion is used as described in section 4.3. The internal

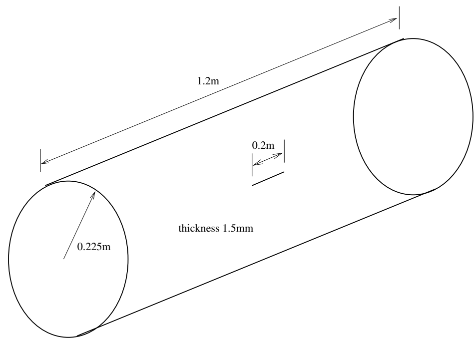

Figure 4: Dimension of the pressurized cylinder problem

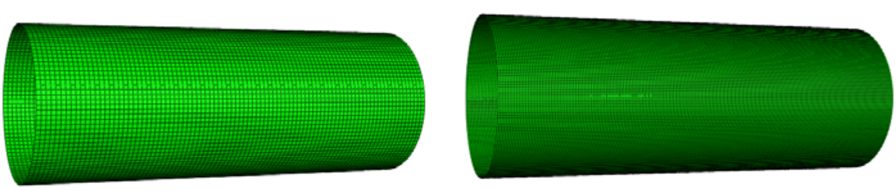

(a) 30,000 nodes (b) 150,000 nodes

Figure 5: Structured nodal arrangement and background mesh of the pressurized cylinder problem; initial configuration

pressure is increased linearly. We test 2 scenarios:

- slow loading rate
- fast loading rate

For slow loading rate, we perform quasi static analysis and the loading rate is $15.2 Pa/s$. For fast loading rate, the maximum load of 15.2MPA is reached after $1 ms$ leading to loading rate of $15.2 kPa/s$.

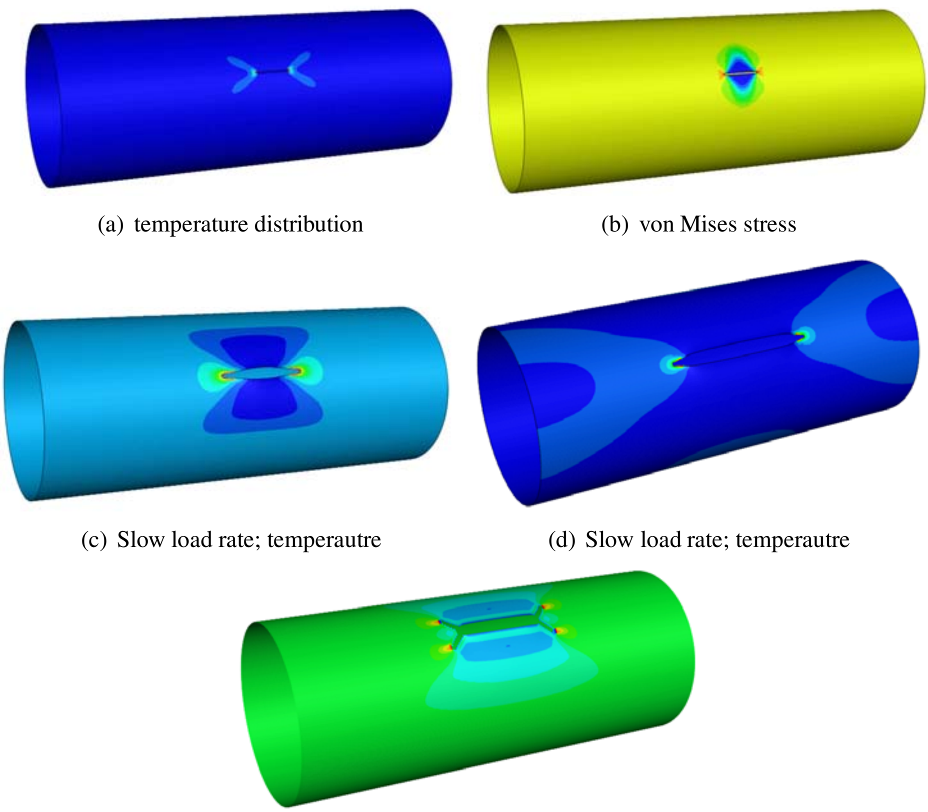

(a) temperature distribution

(b) von Mises stress

(c) Slow load rate; temperautre

(d) Slow load rate; temperautre

(e) Fast load rate; von Mises stress

Figure 6: Displaced configuration of the cylinder under internal pressure

The displaced cylinder for slow loading rate is illustrated in figure 6. The crack propagates straight. For fast loading rate, the crack propagates first straight but then branches. This was also observed by other authors Zhou, Ravichandran, and Rosakis (1996); Ravi-Chandar (1998); Sharon, Gross, and Fineberg (1995);

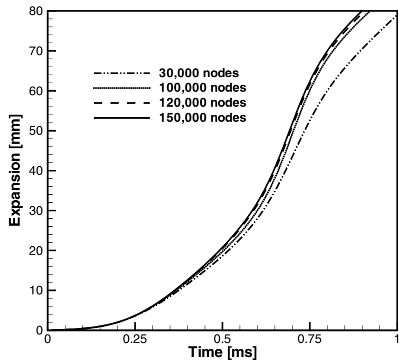

Figure 7: Maximum radial displacements for different meshes

Rabczuk and Belytschko (2004, 2007). The maximum radial displacements measured from the simulation data for different meshes are shown in figure 7. The results are almost indistinguishable after exceeding 100,000 nodes. This indicates mesh independent results. The displaced cylinder and the crack patterns are also indistinguishable and therefore we presented only the displaced cylinder for the simulation with 100,000 nodes in figure 6.

5.3 Detonation driven fracture of cylinder

This problem was experimentally studied by Chao (2004). The test-setup consists of a detonation tube of 152cm length to which a thin-walled aluminium tube is attached. The lengths of aluminium tube range from 45.7cm to 89.6cm. The inner tube radius is 1.975cm and thickness of shell is 0.89mm. While the lower end of the device is closed, a thin diaphragm seals up the other end. The aluminium tube contains notches of various lengths midspan of the aluminium tube. The entire apparatus is filled with a combustible mixture of ethylene and oxygen. Initial pressure varies from 80kPa to 180kPa. The mixture is thermally ignited at the closed end and the combustion transitions quickly to a detonation. When it enters the test specimen, the detonation is close to the Chapman-Jouguet (CJ) limit of quasi-stationary self-sustained propagation. Its velocity is between 2300m/s and 2400m/s and the pressure values in the fully recreated CJ state range from 2.6MPa to 6.1MPa (depending on the initial pressure).

We model this problem with von Mises type J_2 visco-plasticity model, section 4.1, and strain-based failure criterion. The material data is: $E = 69GPa$, $\rho =$

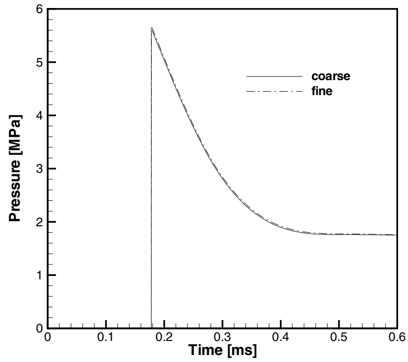

Figure 8: Pressure over the time of a particle close to the notch from a pure fluid simulation of gas-detonation in rigid specimen

$2719kg/m^3$, $\nu = 0.33$, $\sigma_0 = 275GPa$, $\varepsilon_0^p = 0.001$, $1/n = 0.07$, $1/m = 0.01$. Since it is complicated to model the gas explosion and fracture of the cylinder at the same time, we proceed as follows:

- We first simulate the gas explosion at rigid cylinder.
- Then, we prescribe the pressure time history of the previous simulation to our fracture model.

The gas explosion simulation was done by using equation of state model. The pressure time-history at the notch location of one particle is shown in figure 8. We now focus on the fracture of the shell. More details on the gas explosion simulation is given in Gato (2007).

The cylindrical shells are modeled with up to 280,000 nodes. Using half the number of nodes resulted in similar numerical data. We considered 2 notch lengths.

For notch length of 1", the results are shown in figure 9. Cracks propagate shortly from the crack tips and then bifurcate in circumferential direction. Similar observations were made in the experiment. The cracks are arrested after propagating approximately 3/4 of the circumference. In the experiment, the side opposed to the source of explosions failed around the entire circumference while the other side did not. The simulation cannot capture this behavior due to the relatively regularly applied pressure load. A coupled simulation might resolve this issue.

For notch length of 2", result is shown in figure 10. Since pressure differences

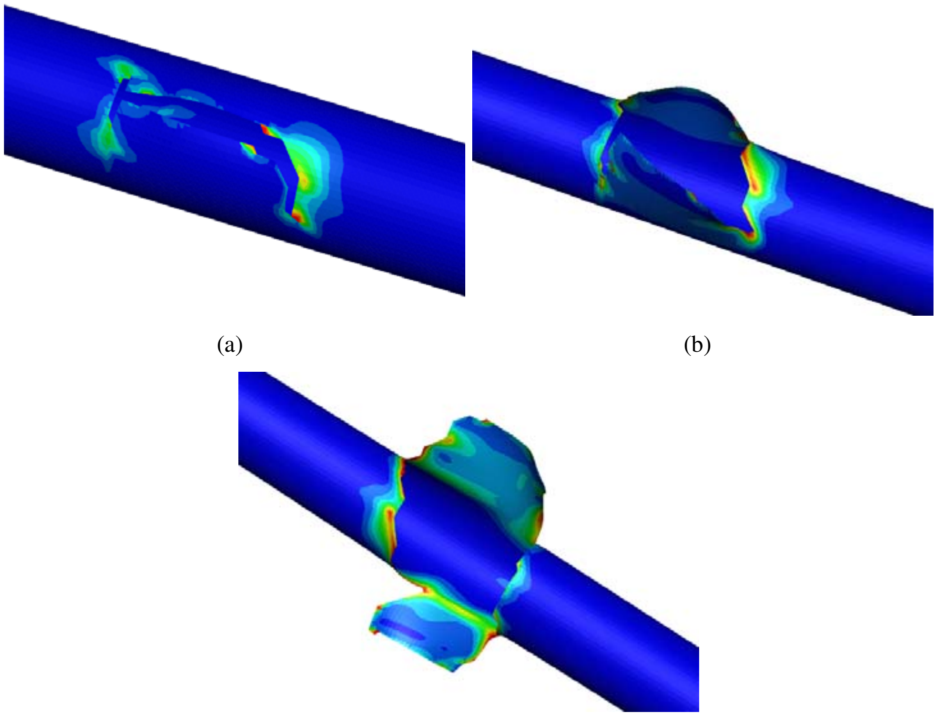

(a) (b)

(c)

Figure 9: Displaced configuration and effective stress of the detonation-driven fracture of cylinder at different times; notch length is 1”

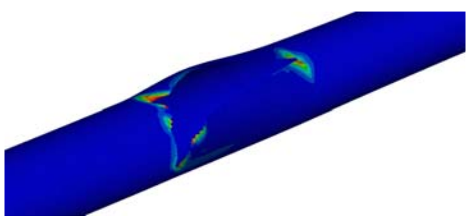

(a)

Figure 10: Displaced configuration and effective stress of the detonation-driven fracture of cylinder; notch length is 2”

around and ahead of the crack tips were more pronounced from the gas explosion simulations, we captured the basic behavior of the experiment. While crack propagates straight on the RHS, crack curves in 45 degree angle before propagating in circumferential direction and getting arrested. This behavior was also seen in the experiment.

6 Conclusions

With the developments of a non-linear meshfree method and a thermo-visco-plastic material model, we studied the failure of cylinders. The advantages of using a meshfree method over finite element method are:

- Meshfree method can deal with large deformations more accurately than finite element method.
- Arbitrary crack growth is represented naturally and independent of the nodal arrangement because of absence of mesh.
- No complicated shell theory needs to be used that is difficult to implement. Nevertheless, the results are of the same accuracy for similar amount of nodes.

We predicted the failure mode of cylinders under internal pressure independent of the mesh size (after exceeding 100,000 nodes). We modeled detonation-driven fracture of cylindrical tubes with different notch lengthes. Therefore, internal pressure time histories from pure gas-detonation fluid simulation in rigid tube is used. For notch length of 2”, experimental fracture pattern can be predicted accurately while for notch length of 1”, our simulated fracture pattern is different from the experimental fracture pattern though we were able to predict the basic features, i.e. crack bifurcation in circumferential direction and short straight crack propagation. These differences might occur due to neglecting fluid-structure interaction effect. For short notch, spatial pressure distribution around and ahead the notch is similar in simulation of pure fluid simulation while spatial differences in pressure distribution occur for longer notch length. A more sophisticated fracture model might be another source of inaccuracies. Discrete crack cohesive zone model will improve accuracy. These aspects will be studied in future research.

References

Andreaus, U.; Batra, B.; Porfiri, M. (2005): Vibrations of cracked euler-bernoulli beams using meshless local petrov-galerkin (mlpg) method. *CMES: Computer Modeling in Engineering & Sciences*, vol. 9, pp. 111–131.

Atluri, S. (2002): *The Meshless Local Petrov-Galerkin (MLPG) Method.* Tech Science Press.

Atluri, S.; Cho, J.; Kim, H. (1999): Analysis of thin beams, using the meshless local petrov-galerkin method, with generalized moving least-squares interpolations. *Computational Mechanics*, vol. 24, pp. 334–347.

Atluri, S.; Shen, S. (2002): The meshless local petrov-galerkin method: a simple and less-costly alternative to the finite element and boundary element methods. *CMES: Computer Modelling in Engineering and Sciences*, vol. 3, pp. 11–51.

Atluri, S.; Zhu, T. (1998): A new meshless local petrov-galerkin (mlpg) approach in computational mechanics. *Computational Mechanics*, vol. 22, pp. 117–127.

Atluri, S.; Zhu, T. (2000): The meshless local petrov-galerkin (mlpg) approach for solving problems in elasto-statics. *Computational Mechanics*, vol. 25, pp. 169–179.

Belytschko, T.; Lu, Y. (1995): Element-free galerkin methods for static and dynamic fracture. *International Journal of Solids and Structures*, vol. 32, pp. 2547–2570.

Belytschko, T.; Lu, Y.; Gu, L. (1994): Element-free galerkin methods. *International Journal for Numerical Methods in Engineering*, vol. 37, pp. 229–256.

Belytschko, T.; Lu, Y.; Gu, L. (1995): Crack propagation by element-free galerkin methods. *Engineering Fracture Mechanics*, vol. 51, no. 2, pp. 295–315.

Bucalem, M.; Bathe, K.-J. (1993): Higher-order mitc general shell elements. *International Journal for Numerical Methods in Engineering*, vol. 36, pp. 3729–3754.

Chao, T. (2004): Gaseous detonation-driven fracture of tubes. *PhD thesis, California Institute of Technology.*

Donning, B.; Liu, W. (1998): Meshless methods for shear-deformable beams and plates. *Computer Methods in Applied Mechanics and Engineering*, vol. 152, no. 1-2, pp. 47–71.

Fujimoto, T.; Nishioka, T. (2006): Numerical simulation of dynamic elasto visco-plastic fracture using moving finite element method. *CMES: Computer Modeling in Engineering & Sciences*, vol. 11, no. 2, pp. 91–101.

Gao, L.; Liu, K.; Liu, Y. (2006): Applications of mlpg method in dynamic fracture problems. *CMES: Computer Modeling in Engineering & Sciences*, vol. 12, no. 3, pp. 181–195.

Gato, C. (2007): Numerical analysis of cylindrical shell fracture. *PhD thesis, Harbin Engineering University*.

Guo, Y.; Nairn, J. (2006): Three-dimensional dynamic fracture analysis using the material point method. *CMES: Computer Modeling in Engineering & Sciences*, vol. 16, no. 3, pp. 141–155.

Guz, A.; Menshykov, O.; Zozulya, V. (2007): Contact problem for the flat elliptical crack under normally incident shear wave. *CMES: Computer Modeling in Engineering & Sciences*, vol. 17, no. 3, pp. 205–214.

Hagihara, S.; Tsunori, M.; Ikeda, T. (2007): Application of meshfree method to elastic-plastic fracture mechanics parameter analysis. *CMES: Computer Modeling in Engineering & Sciences*, vol. 17, no. 2, pp. 63–72.

Han, Z.; Atluri, S. (2003): Truly meshless local petrov-galerkin (mlpg) solutions of traction and displacement bies. *CMES: Computer Modelling in Engineering and Sciences*, vol. 4, pp. 665–678.

Hao, S.; Liu, W. (1999): Bimaterial interfacial crack growth with strain gradient theory. *Journal of Engineering Materials and Technology-Transactions of the ASME*, vol. 121, pp. 413–421.

Hao, S.; Liu, W. (2006): Moving particle finite element method with superconvergence: Nodal integration formulation and applications. *Computer Methods in Applied Mechanics and Engineering*, vol. 195, pp. 6059–6072.

Hao, S.; Liu, W.; Belytschko, T. (2004): Moving particle finite element method with global smoothness. *International Journal for Numerical Methods in Engineering*, vol. 59, pp. 1007–1020.

Hao, S.; Liu, W.; Chang, C. (2000): Computer implementation of damage models by finite element and meshfree methods. *Computer Methods in Applied Mechanics and Engineering*, vol. 187, pp. 401–440.

Hao, s.; Liu, W.; Klein, P.; Rosakis, A. (2004): Modeling and simulation of intersonic crack growth. *International Journal of Solids and Structures*, vol. 41, no. 7, pp. 1773–1799.

Hao, S.; Liu, W.; Moran, B.; Olson, G. (2003): A hierarchical multi-physics model for design of high toughness steels. *Journal of Computer-Aided Materials Design*, vol. 10, pp. 99–142.

Hao, S.; Liu, W.; Moran, B.; Vernerey, F.; Olson, G. (2004): Multi-scale constitutive model and computational framework for the design of ultra-high strength, high toughness steels. *Computer Methods in Applied Mechanics and Engineering*, vol. 193, pp. 1865–1908.

Hao, S.; Liu, W.; Weertman, J. (2004): Cohesive solutions of intersonic moving dislocations. *Philisophical Magazine*, vol. 84, pp. 1067–1104.

Jarak, T.; Soric, J.; Hostler, H. (2007): Analysis of shell deformation repsonses by the meshless local petrov-galerkin (mlpg) approach. *CMES: Computer Modeling in Engineering & Sciences*, vol. 18, no. 3, pp. 235–246.

Jiawei, X.; Xuefeng, C.; Lianfa, Y. (2008): A class of wavelet-based flat shell elements using b-spline wavelet on the interval and its applications. *CMES: Computer Modeling in Engineering & Sciences*, vol. 23, no. 1, pp. 1–12.

Ju, S.; Liu, S. (2007): Determining stress intensity factors of composites using crack opening displacement. *Composite Structures*, vol. 81, pp. 614–621.

Kanok-Nukulchai, W.; Barry, W.; Saran-Yasoontorn, K.; Bouillards, P. (2001): On elimination of shear locking in the element-free galerkin method. *International Journal for Numerical Methods in Engineering*, vol. 52, pp. 705–725.

Krysl, P.; Belytschko, T. (1996): Analysis of thin shells by the element-free galerkin method. *International Journal for Numerical Methods in ENgineering*, vol. 33, pp. 3057–3078.

Lancaster, P.; Salkauskas, K. (1981): Surfaces generated by moving least squares methods. *Mathematics and Computation*, vol. 37, pp. 141–158.

Le, P.; Mai-Duy, N.; Tran-Cong, T. (2008): A meshless modeling of dynamic strain localization in quasi-brittle materials using radial basis function networks. *CMES: Computer Modeling in Engineering & Sciences*, vol. 25, no. 1, pp. 43–67.

Leitao, V. (2001): A meshless method for kirchhoff plate bending problems. *International Journal for Numerical Methods in Engineering*, vol. 52, pp. 1197–1130.

Li, Q.; Soric, J.; Jarak, T.; Atluri, S. (2005): A locking-free meshless local petrov-galerkin (mlpg) formulation for thick and thin plates. *Journal of Computational Physics*, vol. 208, no. 1, pp. 116–133.

Li, S.; Hao, W.; Liu, W. (2000): Numerical simulations of large deformation of thin shell structures using meshfree methods. *Computational Mechanics*, vol. 25, pp. 102–116.

Liew, K.; Chen, X. (2004): Buckling of rectangular mindlin plates subjected to partial in-plane edge loads using the radial point interpolation method. *International Journal of Solids and Structures*, vol. 41, pp. 1677–1695.

Liew, K.; Chen, X. (2004): Mesh-free radial point interpolation method for the buckling analysis of mindlin plates. *International Journal for Numerical Methods in Engineering*, vol. 60, pp. 1961–1877.

Liu, H.; Han, Z.; Rajendran, A.; Atluri, S. (2006): Computational modeling of impact response with the rg damage model and the meshless local petrov-galerkin (mlpg) approaches. *CMC: Computers Materials and Continua*, vol. 4, pp. 43–53.

Liu, W.; Jun, S.; Zhang, Y. (1995): Reproducing kernel particle methods. *International Journal for Numerical Methods in Engineering*, vol. 20, pp. 1081–1106.

Liu, Y.; Liu, L.; Mahadevan, S. (2007): Analysis of subsurface crack propagation under rolling contact loading in railroad wheels using fem. *Engineering Fracture Mechanics*, vol. 17, pp. 2659–2674.

Long, S.; Atluri, S. (2002): A meshless local petrov-galerkin method for solving the bending problem of a thin plate. *CMES: Computer Modeling in Engineering and Sciences*, vol. 3, pp. 53–63.

Ma, J.; Lu, H.; Wang, B. (2006): Multiscale simulation using generalized interpolation material point (gimp) method and molecular dynamics (md). *CMES: Computer Modeling in Engineering & Sciences*, vol. 14, no. 2, pp. 101–117.

Nguyen-Van, H.; N, N. M.-D.; Tran-Cong, T. (2008): A smoothed four-node piezoelectric element for analysis of two-dimensional smart structures. *CMES: Computer Modeling in Engineering & Sciences*, vol. 23, no. 3, pp. 209–222.

Nishioka, T. (2005): Recent advances in numerical simulation technologies for various dynamic fracture phenomena. *CMES: Computer Modeling in Engineering & Sciences*, vol. 10, no. 3, pp. 209–215.

Nishioka, T.; Kobayashi, Y.; Fujimoto, T. (2007): The moving finite element method based on delaunay automatic triangulation for fracture path prediction simulations in nonlinear elastic-plastic materials. *CMES: Computer Modeling in Engineering & Sciences*, vol. 17, no. 3, pp. 231–238.

Noguchi, H.; Kawashima, T.; Miyamura, T. (2000): Element free analysis of shell and spatial structures. *International Journal for Numerical Methods in Engineering*, vol. 47, pp. 1215–1240.

Parish, H. (1991): An investigation of a finite rotation four node assumed strain shell element. *International Journal for Numerical Methods in Engineering*, vol. 31, pp. 127–150.

Peirce, D.; Shih, C.; Needleman, A. (1984): A tangent modulus method for rate dependent solids. *Computers and Structures*, vol. 18, pp. 875–887.

Rabczuk, T.; Areias, P. (2006): A meshfree thin shell for arbitrary evolving cracks based on an extrinsic basis. *CMES: Computer Modeling in Engineering & Sciences*, vol. 16, no. 2, pp. 115–130.

Rabczuk, T.; Areias, P.; Belytschko, T. (2007): A meshfree thin shell method for non-linear dynamic fracture. *International Journal for Numerical Methods in Engineering*, vol. 72, no. 5, pp. 524–548.

Rabczuk, T.; Belytschko, T. (2004): Cracking particles: A simplified meshfree method for arbitrary evolving cracks. *International Journal for Numerical Methods in Engineering*, vol. 61, no. 13, pp. 2316–2343.

Rabczuk, T.; Belytschko, T. (2005): Adaptivity for structured meshfree particle methods in 2d and 3d. *International Journal for Numerical Methods in Engineering*, vol. 63, no. 11, pp. 1559–1582.

Rabczuk, T.; Belytschko, T. (2006): Application of particle methods to static fracture of reinforced concrete structures. *International Journal of Fracture*, vol. 137, no. 1-4, pp. 19–49.

Rabczuk, T.; Belytschko, T. (2007): A three-dimensional large deformation meshfree method for arbitrary evolving cracks. *Computer Methods in Applied Mechanics and Engineering*, vol. 196, no. 29-30, pp. 2777–2799.

Rabczuk, T.; Belytschko, T.; Xiao, S. (2004): Stable particle methods based on lagrangian kernels. *Computer Methods in Applied Mechanics and Engineering*, vol. 193, pp. 1035–1063.

Rabczuk, T.; PMA, P. A.; Belytschko, T. (2007): A simplified mesh-free method for shear bands with cohesive surfaces. *International Journal for Numerical Methods in Engineering*, vol. 69, no. 5, pp. 993–1021.

Rabczuk, T.; Zi, G. (2007): A meshfree method based on the local partition of unity for cohesive cracks. *Computational Mechanics*, vol. 39, no. 6, pp. 743–760.

Ravi-Chandar, K. (1998): Dynamic fracture of nominally brittle materials. *International Journal of Fracture*, vol. 90, pp. 83–102.

Rong, F.; Huang, C.; Liu, Z.; Song, D.; Wang, Q. (2008): Microstructure changes in the catalyst layers of pem fuel cells induced by load cycling: Part i. mechanical model. *Journal of Power Sources*, vol. 175, pp. 699–711.

Sharon, E.; Gross, P.; Fineberg, J. (1995): Local crack branching as a mechanism for instability in dynamic fracture. *Physical Review Letters*, vol. 74, pp. 5096–5099.

Simo, J.; Fox, D.; Rifai, M. (1989): On a stress resultant geometrically exact shell model. part ii: The linear theory; computational aspects. *Computer Methods in Applied Mechanics and Engineering*, vol. 73, pp. 53–92.

Sladek, J.; Sladek, V.; Solek, P. (2008): Thermal bending of reissner-mindlin plates by the mlpg. *CMES: Computer Modeling in Engineering & Sciences*, vol. 28, no. 1, pp. 57–76.

Sladek, J.; Sladek, V.; Wen, P.; Aliabadi, M. (2006): Meshless local petrov-galerkin method for shear deformable shell analysis. *CMES: Computer Modeling in Engineering & Sciences*, vol. 13, no. 2, pp. 103–117.

Soric, J.; Li, Q.; Jarak, T.; Atluri, S. (2004): Meshless local petrov-galerkin (mlpg) formulation for analysis of thick plates. *CMES: Computer Modeling in Engineering & Sciences*, vol. 6, no. 4, pp. 349–357.

Sze, K.; Lo, S.; Yao, L. (2002): Hybrid-stress solid elements for shell structures based upon a modified variational functional. *International Journal for Numerical Methods in Engineering*, vol. 53, pp. 2617–2642.

Tang, Z.; Shen, S.; Atluri, N. (2003): Analysis of materials with strain-gradient effects: A meshless local petrov-galerkin(mlpg) approach, with nodal displacements only. *CMES: Computer Modelling in Engineering and Sciences*, vol. 4, pp. 177–196.

Wang, D.; Chen, J. (2006): A locking-free meshfree curved beam formulation with the stabilized conforming nodal integration. *Computational Mechanics*, vol. 39, no. 1, pp. 83–90.

Weissmann, S. (1996): High-accuracy low-order three-dimensional brick element. *International Journal for Numerical Methods in Engineering*, vol. 39, pp. 2337–2361.

Yagawa, G.; Miyamura, T. (2005): 3-node triangular shell element using mixed formulation and its implementation by free mesh method. *Computers and Structures*, vol. 83, pp. 2066–2076.

Zhao, J.; Liu, R.; Wu, X. (2008): Effects of partial crack-face contact for the bending of thin shell structures. *Theoretical and Applied Fracture Mechanics*, vol. 49, pp. 128–150.

Zhou, M.; Ravichandran, G.; Rosakis, A. (1996): Dynamically propagating shear bands in impact-loaded prenotched plates, 2. numerical simulations. *Journal of the Mechanics and Physics of Solids*, vol. 44, no. 6, pp. 1007–1032.